Ni doping in unit cell of BiOBr to increase dipole moment and induce spin polarization for promoting CO_2 photoreduction via enhanced build-in electric field

Yiqiao Wang [a], Yu Xie [a,*], Shuohan Yu [a], Kai Yang [b], Yi Shao [c], Laixi Zou [b], Boxiao Zhao [a], Zilin Wang [a], Yun Ling [a], Yong Chen [a]

[a] *College of Environment and Chemical Engineering, Nanchang Hangkong University, Nanchang 330063, China*
[b] *School of Chemistry and Chemical Engineering, Jiangxi University of Science and Technology, Ganzhou 341000, China*
[c] *The First Affiliated Hospital, Nanchang University, Nanchang 330006, China*

ARTICLE INFO

ABSTRACT

The weak bulit-in electric field of BiOBr material is difficult to promote electron-hole separation, resulting in low photocatalytic CO_2 reduction performance. In this work, Ni has been successfully doped in unit cell of BiOBr and increase the unit cell dipole moment of BiOBr along the x, z directions from 0 to 0.04768 and 0.11293 eÅ, respectively. Enhancement of the unit cell dipole moment induces electron spin polarization near the Fermi energy level, which increases the surface potential from 18 mV to 36.2 mV. When the Ni doping ratio is 3 %, a higher carrier separation efficiency is achieved. 3 %Ni-BiOBr has the excellent CO_2 photoreduction performance with CO yield of 378.7 $\mu molg^{-1}h^{-1}$, which is 4.3 times higher than pure BiOBr (86.75 $\mu molg^{-1}h^{-1}$). Briefly, this research work throws light on enhancing built-in electric field by increasing unit cell dipole moment and inducing spin polarization for improving the photocatalytic performance.

1. Introduction

Converting CO_2 into fuels and chemical feedstocks not only mitigates the global greenhouse effect but also reduces humans' over-reliance on fossil fuels [1–4]. Solar-driven semiconductor photocatalytic reduction of CO_2 is a great interest because it is environmentally friendly and sustainable [5–8]. However, compared to transfer to surface and the surface reaction, the photogenerated electrons and holes in the photocatalysis were easier to recombination in the bulk of catalyst, which seriously limited the photocatalytic performance [9–11]. Therefore, it is imperative to explore strategies to promote electron-hole separation [12–14].

Over the decades, a range of materials have been developed for sunlight-driven CO_2 reduction, such as TiO_2, C_3N_4, CdS and MOFs. But for a variety of reasons, they have not been achieved the desired results [15–18]. BiOBr is a typical semiconductor material favoured due to its excellent visible light response and suitable energy band position. However, the fast photo-generated electron-hole complexation and the small number of reactive sites lead to poor photocatalytic performance [19,20]. It has been widely reported that altering electronic structure of BiOBr to enhance photocatalytic activity by the entry of some major elements into the lattice of BiOB [21,22]. VB of BiOX (X = Cl, Br, I) was composed of O 2p and X np (n = 3, 4, 5) orbitals, CB was dominated by Bi 6p orbitals, which had similar layered crystal structure. Therefore, it was easy to adjust IEF by changing the unit cell structures [23,24].

However, there are no reports on the doping of transition metals into BiOBr to enhance the photocatalytic reduction of CO_2 [25]. The doping of transition metals into the unit cell of BiOBr generates built-in electric field (IEF), which is profitable to the generate more photogenerated carriers even at lower absorption energies [26]. IEF can also act as a springboard for electrons to leap from the VB to the CB, which can effectively inhibit electron-hole recombination [27]. At the same time, the formation of IEF preserves the red-shift of the optical absorption band and its structural is stability after elemental doping. This can greatly improve the activity and stability of their photocatalytic reduction of CO_2 to a certain extent.

In this work, a one-step hydrothermal method was used to dope Ni in unit cell of BiOBr. By density functional theory (DFT) calculation and experimental results, it is found that the introduction of Ni causes lattice distortion, which leads to the change of dipole moment and IEF. Kelvin
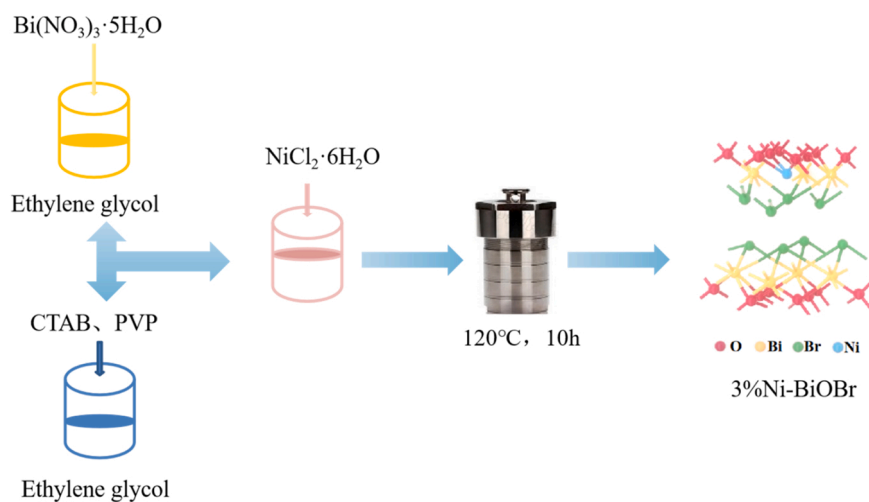

Fig. 1. Schematic illustration of preparation process of 3 %Ni-BiOBr.

Probe atomic force microscopy (KPFM) and Zeta potential tests confirmed the results. This study plays an important role in the polarization induced by element doping and charge separation, and opens a new horizon for the construction of semiconductors with strong built in electric field.

2. Experimental

2.1. Preparation of Ni-doped flower-like BiOBr

Firstly, 4 mmol $Bi(NO_3)_3 \cdot 5H_2O$ was dissolved in 25 mL of ethylene glycol and the solution was stirred for 1 h, named as solution A. 4 mmol cetyltrimethylammonium bromide (CTAB) and 5 mg PVP were dissolved in 25 mL of ethylene glycol and the solution was stirred for 1 h, named as solution B. Then, solution A was slowly added to solution B with stirring. Secondly, different masses of $NiCl_2 \cdot 6H_2O$ were added to the above solution subsequently and sonicated for 5 min. Then the suspension was transferred to a reactor and heated hydrothermally at 120 °C for 10 h, and cooled down to room temperature. The samples were washed three times with DI water and dried in a vacuum drying oven. The samples were named 1 %Ni-BiOBr, 3 %Ni-BiOBr and 5 %Ni-BiOBr according to the mass fraction of Ni element. As comparsion, pure BiOBr was obtained under the same condition. The detailed synthesis steps were shown in Fig. 1.

2.2. Characterization

X-ray diffractometry (XRD, Cu Kα-ray) was used to analyze the crystal structure of the samples with a scanning angle of $10° - 70°$ and a scan speed of 6°/min. Fourier infrared spectroscopy (FT-IR, Thermofisin10 iZ10) and Raman spectroscopy (Raman) were employed to investigate the successful introduction of the Ni element. Scanning electron microscopy (SEM, Nova NaNoSEM450), transmission electron microscopy (TEM, FEI Talos F200X) and HRTEM were applied to study the microstructure and elemental distribution of the samples. X-ray photoelectron spectroscopy (XPS, Axis Ultra DLD) was used to analyze the elemental state of the sample surface. The surface potential of the sample was measured in the AFM Kelvin probe mode (KPFM Bruker Dimension Icon). The zeta potential of the samples was determined by Nanobrook 90Plus PALS potential analyzer. The fluorescence emission intensity of the material was tested using a fluorescence emitter (PL, Hitachi F4500) under 380 nm excitation light. Time-resolved photoluminescence (TRPL ISS ChronosBH) was used to probe the fluorescence lifetime of the catalysts. The CO_2 adsorption and conversion processes were measured by in situ diffuse reflectance infrared Fourier transform spectroscopy (DRIFTS) of PerkinElmer Spectrum One.

2.3. CO_2 reduction performance test

The mixture solution of $H_2O/CH_3CN/TEOA$ (1:4:1 total 6 mL), 5 mg $[Ru(bpy)_3]Cl_2 \cdot 6H_2O$ and 5 mg catalyst were added to a 50 mL quartz tube. Then CO_2 was continuously injected into the reactor for 30 min to ensure that the air in the reactor was completely replaced by CO_2. A 300 W xenon lamp with a 380 nm filter ($\lambda \geq 380$ nm) was used as the light source. The reaction process lasted for 3 h under visible light and 500 μL of the final gaseous product was taken for subsequent qualitative analysis by the Pana A91 Plus gas chromatograph equipped with a flame ionisation detector. To test the stability of the catalyst, a distribution strategy was adopted to compensate for the loss of clarity and transfer between cycles. Parallel experiments were performed on 100 mg of catalyst under the same experimental conditions and then collected together. 5 mg were taken out each time for the next test.

2.4. Electrochemical test

The samples were tested electrochemically using an electrochemical workstation (CHI 660D) with a three-electrode system. The test sample was first applied uniformly to a 1 cm² conductive glass (FTO). In the three-electrode system, the sample-coated FTO was used as the working electrode, the Pt electrode as the counter electrode, the Ag/AgCl electrode as the reference electrode and the electrolyte was a 0.1 M Na_2SO_4 solution. In the photocurrent test, the light source was a 300 W xenon lamp which is used in the performance test. The EIS text was tested at frequencies from 0.01 Hz to 100 kHz.

2.5. Computational details

The DMol3 module of the Materials Studio software (Accelrys Inc.) was employed for the quantum chemistry calculations. Based on experimental results, (110) surfaces were chosen to be calculated, the corresponding surfaces were constructed using the lattice parameter optimized for bulk BiOBr (space group: P4/mmm, a=b =3.953 Å, c=8.884 Å , a=β = γ = 90°) with a vacuum region of 15 Å. During the calculations, self-consistent periodic Density Functional Theory (DFT) calculations were performed with the generalized gradient-corrected Perdew–Burke–Ernzerhof (GGA/PBE) functional [28] using a double numerical basis set with polarization function (DNP) [29]. For the electronic coordinates relaxation, the tolerances of energy, maximum force, and maximum displacement were set to be 1.0×10^{-5} Ha, 0.002 Ha/Å and 0.005 Å, respectively. The Monkhorst-Pack k-point
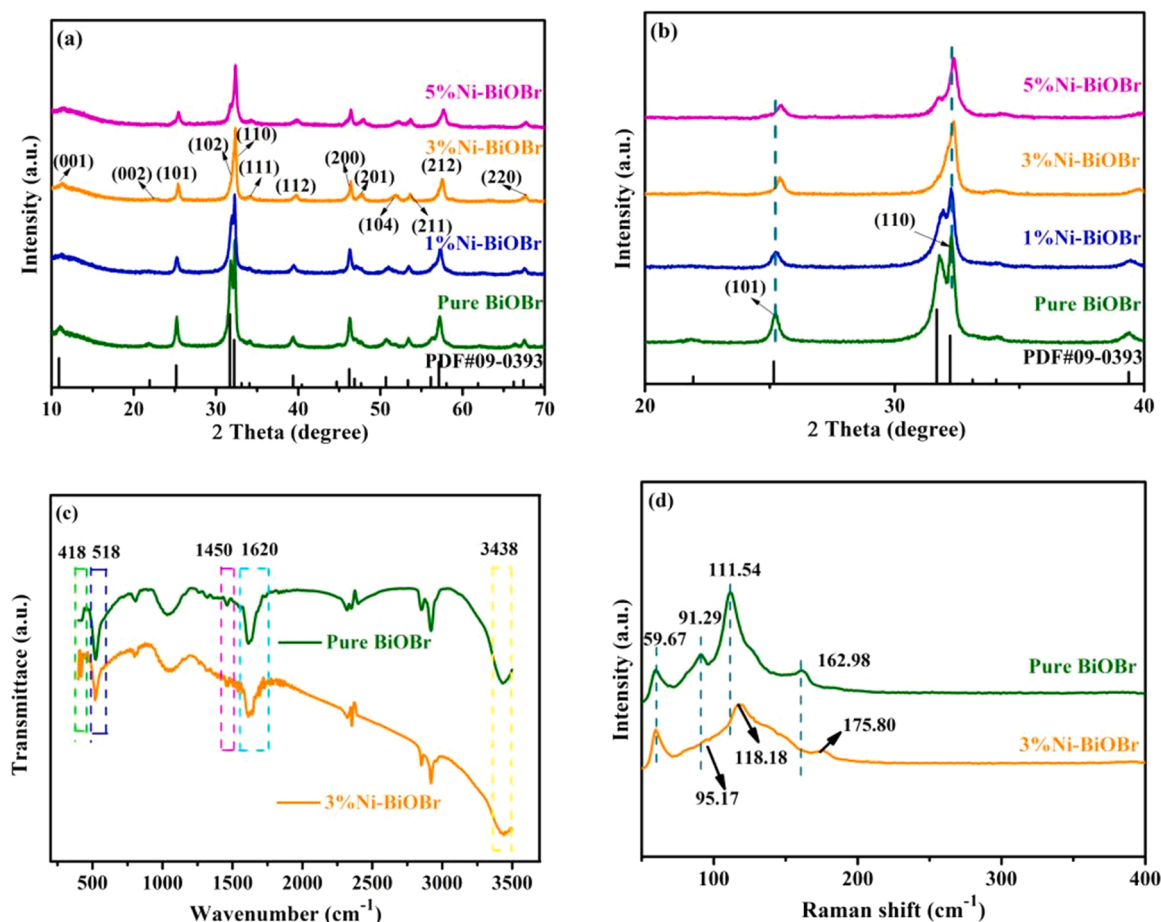
Fig. 2. XRD pattern (a), 2θ = 20–40° enlargement views (b) of all samples; FT-IR spectra (c) and Raman spectra (d) of BiOBr and 3 %Ni-BiOBr.

mesh was set to be $2 \times 2 \times 2$. The $3 \times 3 \times 1$ supercells for bulk and 3×3 for surfaces were constructed to calculate spin DOS and work function through a spin-unrestricted method[30]. For achieving high quality results, the real space global orbital cutoff radius was set as 4.8 Å and the smearing of orbital occupancy was 0.005 Ha.

3. Results and discussion

3.1. Ni doping in unit cell of BiOBr to replace Bi and form N-O bonds

X-ray diffraction (XRD) was used to characterize the crystal structure of the sample and Fig. 2a was obtained. It can be seen that all samples are indexed as tetragonal BiOBr (PDF#09–0393)[31]. There are no other impurity peaks at 3 %Ni-BiOBr, indicating that Ni is highly dispersed. Meanwhile, further observation under the local magnification of 2θ = 20°−40° (Fig. 2b) shows that there is an obvious offset toward higher angle after Ni doping, which implies that Ni is successfully introduced into the cellular matrix of BiOBr. In addition, the diffraction peaks of all Ni-doped samples are consistent with BiOBr, indicating that Ni doping did not significantly change the phase structure.

The Ni doping state was further investigated via FT-IR (Fig. 2c). Where the peak at 3438 cm^{-1} and 1620 cm^{-1} are attributed to O-H stretching vibrations and bending vibrations with water, respectively [32]. The peaks at 1450 cm^{-1} and 518 cm^{-1} are attributed to Bi-Br bonding and Bi-O bonding vibrational stretching of BiOBr [33]. Excitingly, 3 %Ni-BiOBr has an additional vibrational peak at 418 cm^{-1} which belongs to the Ni-O bonding vibration. This indicates that Ni is doped in the BiOBr unit cell and forms Ni-O bonds with lattice oxygen. In addition, Raman spectroscopy identifies the lattice distortion of BiOBr (Fig. 2d). For BiOBr, the peaks at 91.29 cm^{-1} and 162.98 cm^{-1} belong to

the E_g^1 external and E_g^2 internal Bi-Br stretching modes [34]. The Ni doping caused the BiOBr lattice distortion, which resulted in the shift of the Raman spectrum. The internal stretching of E_g^2 with 3 % Ni-BiOBr is shifted toward higher wave numbers compared to BiOBr, indicating that Ni enters the unit cell replacing Bi to form Ni-O bonds, which is consistent with the FT-IR results [35]. The above results provide sufficient evidence for the successful doping of Ni into the lattice to form Ni-O bonds.

The XPS technique was used to analyze the doping state of Ni in 3 % Ni-BiOBr and used the binding energy of C1s at 284.6 eV for charge correction. The peaks of Bi, O, Br and Ni can be observed in the full spectrum of 3 %Ni-BiOBr, which is a proof of the successful doping of Ni (Fig. S1). Fig. 3a shows the fitted curve for Bi 4 f, with the Bi 4 $f_{7/2}$ and Bi 4 $f_{5/2}$ peaks are clearly visible in BiOBr and 3 %Ni-BiOBr clearly visible. The electron binding energies are 158.81 eV and 164.12 eV for BiOBr as well as 158.63 eV and 163.94 eV for 3 %Ni-BiOBr. This indicates that Ni doping does not change the valence state of Bi and both are present as Bi^{3+} [36]. Fig. 3b shows the fitted curves for O 1s with low electron binding energy attributed to lattice oxygen and high electron binding energy attributed to hydroxyl oxygen of water adsorbed on the sample surface[37]. Electron binding energy of lattice oxygen for BiOBr and 3 % Ni-BiOBr are 529.71 eV and 529.57 eV, respectively. The doublet peaks of Br 3d at 67.95 eV and 68.99 eV for BiOBr as well as 67.63 eV and 68.67 eV for 3 %Ni-BiOBr (Fig. 3c), both attributed to Br $3d_{5/2}$ and Br $3d_{3/2}$ [38]. Thought-provokingly, the electron binding energy of Bi 4f, O1s and Br 3d in 3 %Ni-BiOBr shifts to lower electron binding energy compared to BiOBr. This is due to the increase in electron cloud density caused by the entry of small radius Ni into the BiOBr unit cell matrix forming electron enrichment [39]. Besides, according to Fig. 3d, the doublet peaks around the binding energies of 856.15 eV (Ni $2p_{3/2}$) and
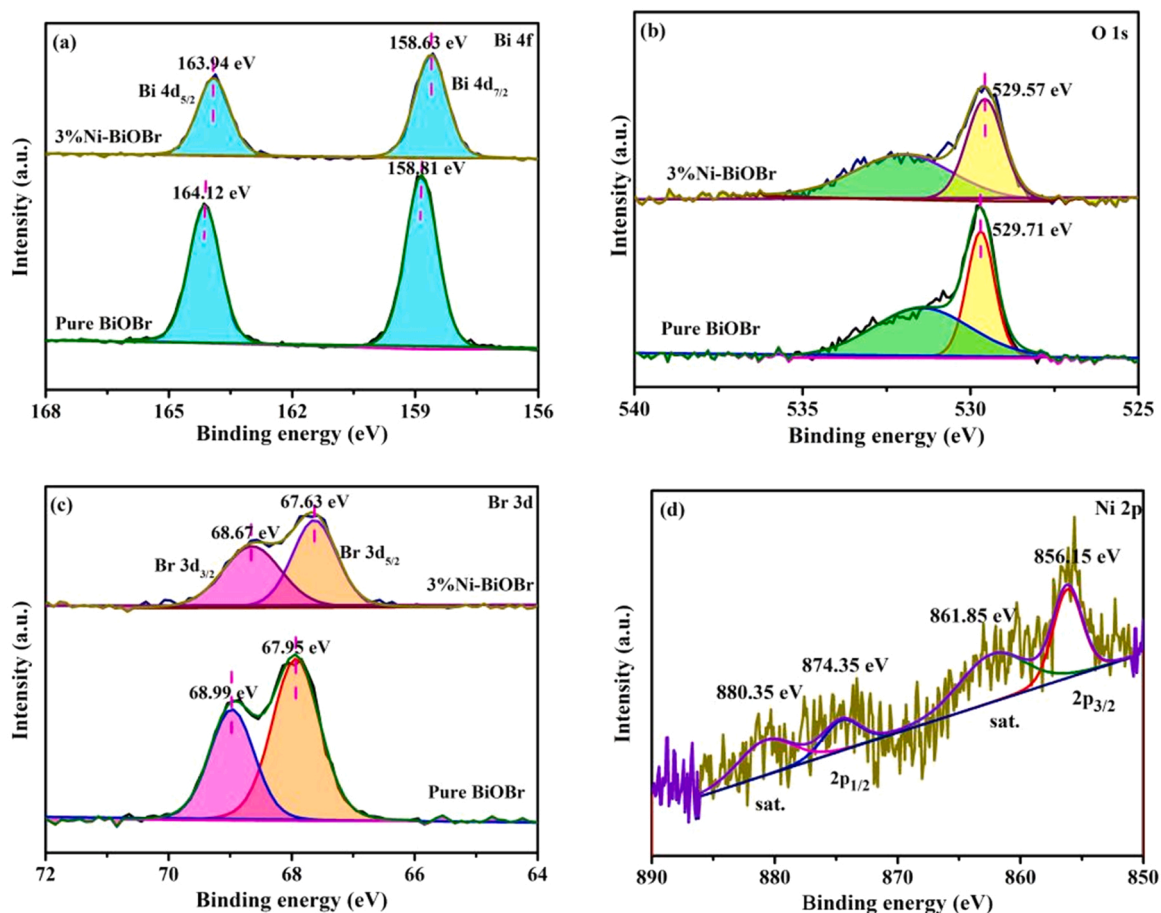
Fig. 3. Bi 4f spectrum (a), O 1s (b) and Br 3d (c) of BiOBr and 3 %Ni-BiOBr; Ni 2p spectrum of 3 %Ni-BiOBr (d).
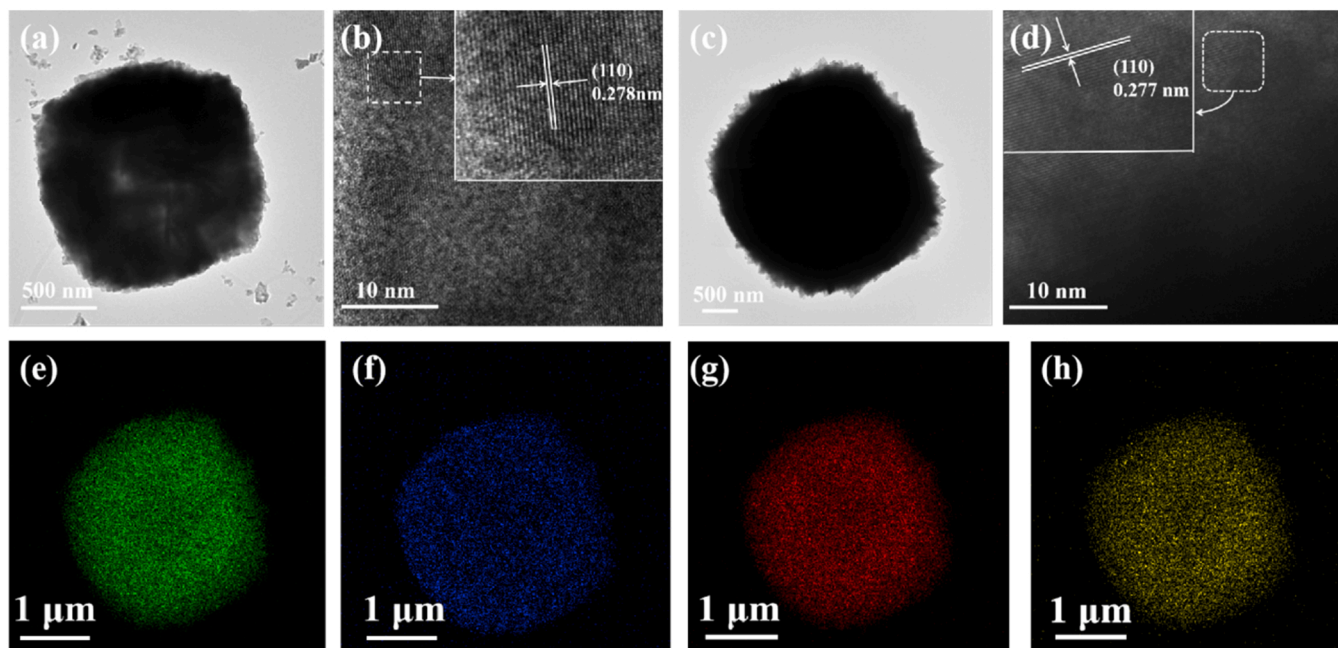

Fig. 4. TEM (a) and HRTEM (b) of BiOBr; TEM (c), HRTEM (d) and the associated elemental mapping Bi (e), O (f), Br (g) and Ni (h) of 3 %Ni-BiOBr.

874.35 eV (Ni $2p_{1/2}$) are corresponded to Ni^{3+}, while the doublet peaks at 861.85. eV and 880.35 eV are attributed to Satellite Peak.

Scanning electron microscopy (SEM), transmission electron microscopy (TEM) and high-resolution transmission electron microscopy (HRTEM) were applied to describe the morphology and Ni element distribution before and after Ni doping. The SEM images of
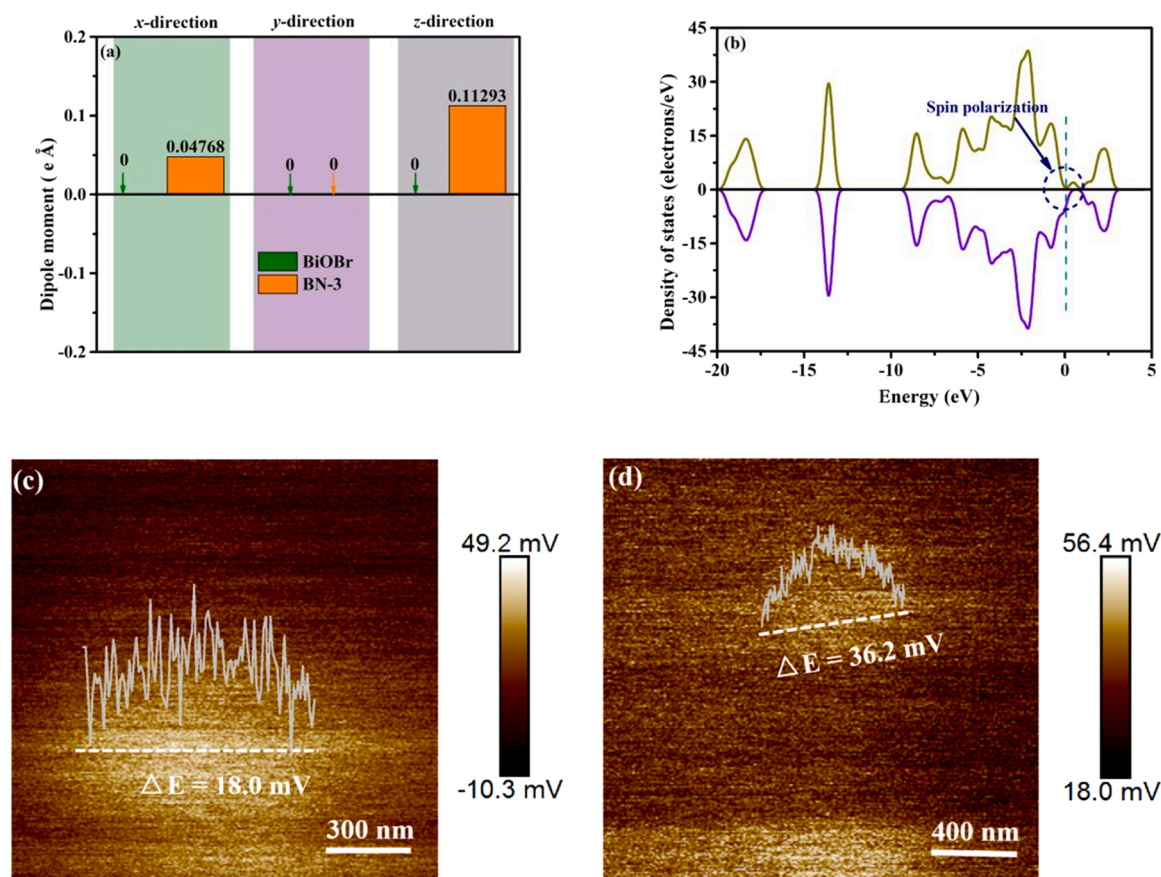
Fig. 5. Theoretical dipole moments for BiOBr and 3 %Ni-BiOBr (a); the calculated total DOS over 3 %Ni-BiOBr (b); KPFM photos of BiOBr (c) and 3 %Ni-BiOBr (d).

BiOBr and 3 %Ni-BiOBr are shown in Fig. S2a and S2b, respectively. It can be obviously seen that both BiOBr and 3 %Ni-BiOBr are flower-like structures formed by nanosheets. From the TEM images (Fig. 4a and c), flower-like structures are observed for both BiOBr and 3 %Ni-BiOBr, which are in agreement with the SEM results. Fig. 4b and d are the HRTEM images of BiOBr and 3 %Ni-BiOBr, respectively. As can be seen, both BiOBr and 3 %Ni-BiOBr show clear lattice stripes, with the (110) crystal plane spacing of 0.278 nm for tetragonal BiOBr as well as 0.277 nm for 3 %Ni-BiOBr. It is noteworthy that the crystal plane spacing of 3 %Ni-BiOBr is smaller than that of BiOBr. This indicates that the lattice constant becomes smaller and confirms the successful doping of Ni into the BiOBr unit cell. Furthermore, the elemental mapping analysis (Fig. 4e-h) shows that Bi, O, Br and Ni are uniformly distributed in 3 %Ni-BiOBr, which proves that Ni is uniformly doped into the BiOBr lattice. In addition, the contents of each element of 3 %Ni-BiOBr are shown in Table S1.

3.2. Enhancement build-in electric field and efficiently carrier separation

To explore the impact of Ni doping on the unit cell dipole moment, calculations were performed for BiOBr and 3 %Ni-BiOBr along three directions (x, y, z). As shown in Fig. 5a, the 3 %Ni-BiOBr unit cell dipole moment increases along the x, z positive directions, which indicates the presence of a strong IEF in 3 %Ni-BiOBr[40]. In addition, the corresponding density of states (DOS) of 3 %Ni-BiOBr (Fig. 5b) shows that 3 %Ni-BiOBr has more self-selected down electrons when the energy is 0. This illustrates that an increase in unit cell dipole moment can induce electron spin polarization and thus enhance the IEF [41]. Meanwhile, KPFM and zeta potential were employed to measure to the samples. As shown in Fig. 5(c-d), the surface potentials of pure BiOBr and 3 % Ni-BiOBr along the white line are 18 mV and 36.2 mV, respectively. It is

clear that the surface potential of 3 %Ni-BiOBr increases after Ni doping. As shown in Fig. S3, the zeta potentials of pure BiOBr and 3 %Ni-BiOBr are −1.91 mV and −25.16 mV, respectively, while the zeta potential of 3 %Ni-BiOBr is much higher than pure BiOBr. The above characterization can fully prove that IEF of the Ni-doped BiOBr was enhanced.

It is well known that the IEF can promote electron-hole separation. To investigate the effect of the enhancement of the IEF on the electron-hole separation, the photocurrent density was measured using transient photocurrent and obtained Fig. 6a. It is obvious that 3 %Ni-BiOBr has higher charge density than BiOBr, which indicates a faster electron-hole separation efficiency. Meanwhile, the charge transfer internal resistance of the catalyst was measured via using electrochemical impedance spectroscopy (EIS). As shown in Fig. 6b, the impedance circle of 3 %Ni-BiOBr is much smaller than that of BiOBr. This indicates that 3 %Ni-BiOBr has lower internal resistance to transfer and faster electron-hole separation efficiency.

The PL spectra of BiOBr and 3 %Ni-BiOBr are shown in Fig. 6c. It is well known that the fluorescence intensity comes from the electron-hole complex, so the electron-hole separation efficiency is inversely proportional to the fluorescence intensity [42]. It is obviously to see that pure BiOBr has the strongest fluorescence intensity and 3 %Ni-BiOBr has the lowest fluorescence intensity. This indicates that the electron-hole separation efficiency of 3 %Ni-BiOBr is improved due to IEF. In addition, we further characterized the time-resolved photoluminescence spectra of pure BiOBr and 3 %Ni-BiOBr were characterized and the results were obtained at Fig. 6d. It is fascinating that 3 %Ni-BiOBr shows a longer fluorescence lifetime compared to pure BiOBr. This further indicates that the enhancement of IEF promotes the electron-hole separation. The above results fully illustrate that IEF enhancement can greatly promote electron-hole separation. Furthermore, from the surface work function, it can be seen from the surface work function (Fig. S4) that 3 %Ni-BiOBr
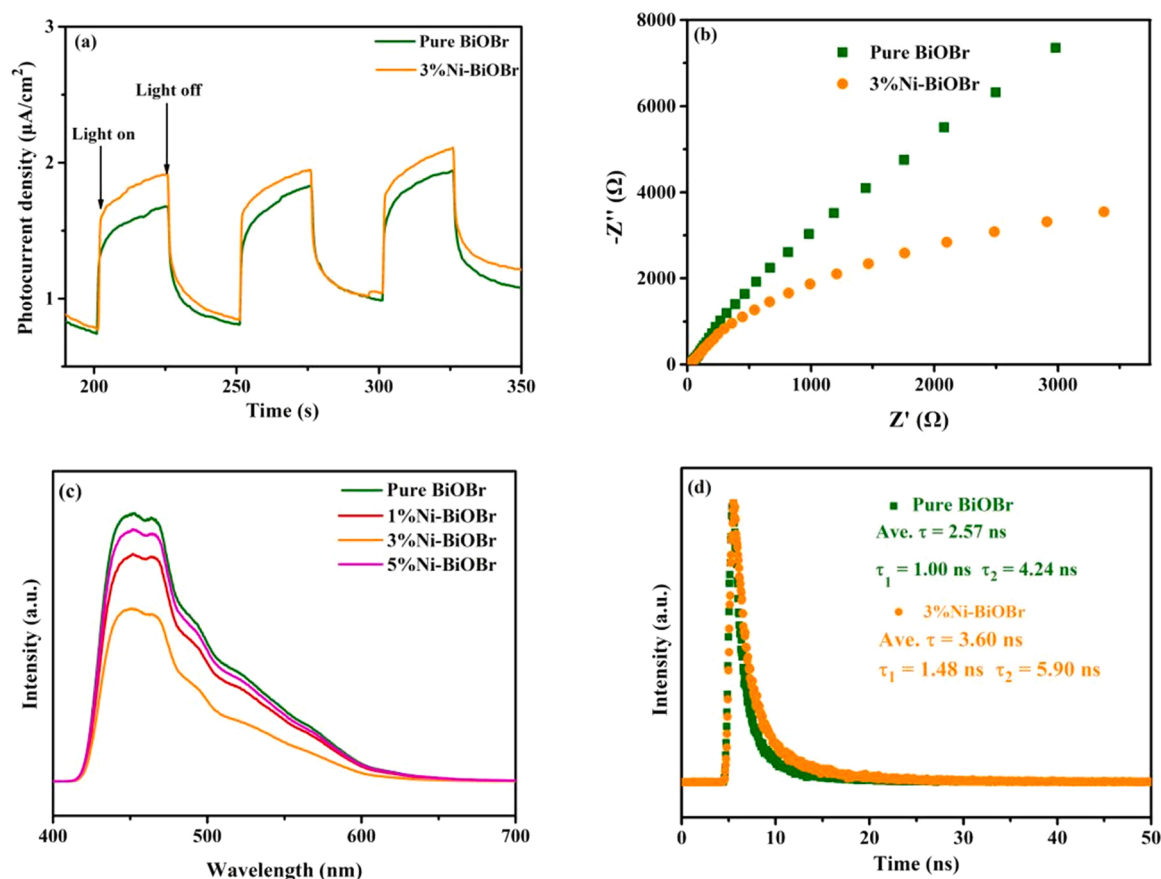
Fig. 6. TPR curves (a), EIS curves (b) and TRPL curves (d) of BiOBr and 3 %Ni-BiOBr; PL spectra (c) of all samples.
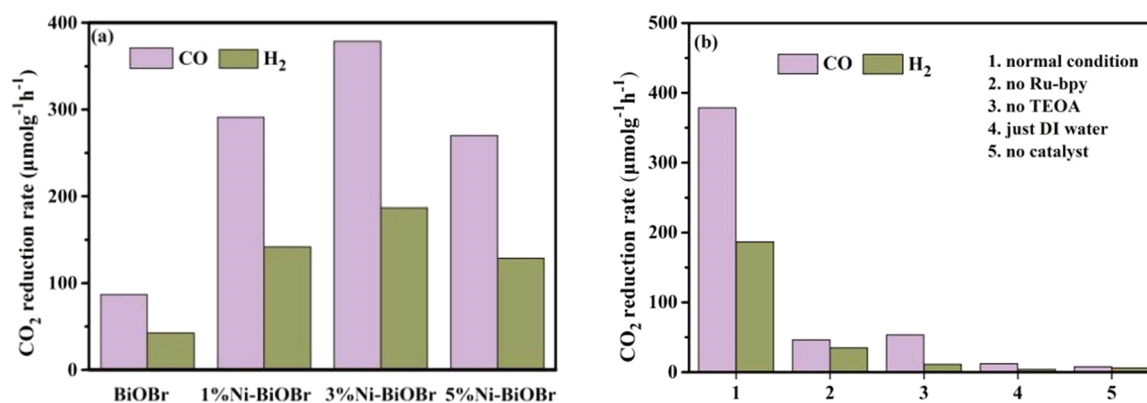

Fig. 7. CO_2 reduction rate of all samples (a) CO_2 photoreduction under various reaction conditions over 3 %Ni-BiOBr(b).

has a lower surface work function. This facilitates the transfer of electrons from the inside to the outside of the material, thus facilitating the occurrence of photocatalytic reactions.

3.3. Ni doped in unit cell of BiOBr to enhance CO_2 photoreduction and the mechanism of charge separation enhancement

In this study, DI water was used as reaction medium. [Ru(bpy)$_3$] Cl$_2$·6H$_2$O (Ru-bpy) functions as an electron donor to provide additional photoelectrons to BiOBr under light conditions and Triethanolamine (TEOA). A 300 W xenon lamp with a 380 nm filter ($\lambda \geq 380$ nm) was used as light source for photocatalytic reduction of CO_2 to evaluate its photocatalytic performance. The products obtained were mainly H$_2$ and

CO, and no liquid products were detected. As shown in Fig. 7a, the CO yield of BiOBr, 1 %Ni-BiOBr, 3 %Ni-BiOBr and 5 %Ni-BiOBr were 86.75, 291.3, 378.7 and 269.95 μmolg^{-1}h^{-1}, respectively. And H$_2$ evolution rate is 42.54, 141.81, 186.84 and 128.46 μmolg^{-1}h^{-1}. It is obvious that 3 %Ni-BiOBr has the best CO evolution rate, which is 4.3 times higher than BiOBr. This indicates that Ni doped in unit cell of BiOBr can significantly improve the performance of photoreduction of CO_2 by enhancing IEF. In addition, compared with previously reported CO_2 photocatalysts, the performance of 3 %Ni-BiOBr is still excellent (Table S2).

As we all know, the experimental conditions are also a key factor affecting the photocatalytic performance. In this study, the effects of sacrificial agent and electron donor were explored as shown in Fig. 7b.
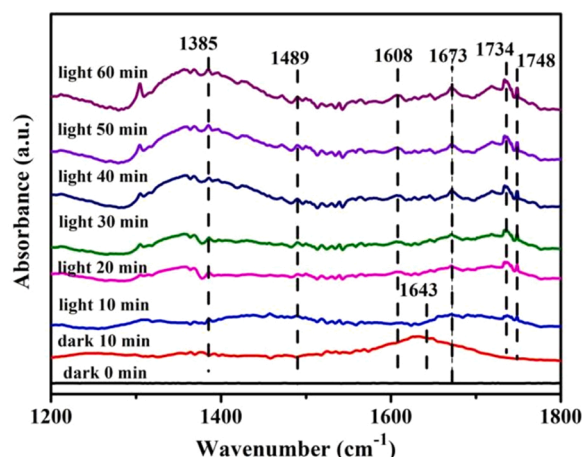
Fig. 8. In situ FT-IR spectra of 3 %Ni-BiOBr.

When the sacrificial agent and electron donor are present simultaneously, it has the best CO and H_2 evolution rate. Surprisingly, when only the sacrificial agent or only the electron donor was present in the reaction system, both CO and H_2 yield decreased dramatically. This suggests that TEOA and electron donors have synergistic effects in photocatalysis. Meanwhile, we performed a blank control on the performance and CO_2 reduction test without the addition of catalyst under conventional test conditions. Its CO_2 reduction performance was only 7.88 $\mu molg^{-1}h^{-1}$, which indicates that 3 %Ni-BiOBr plays an absolute role in the reduction process. In addition, stability is also an important criterion for catalyst performance. The 5 cycles performance of 3 %Ni-BiOBr is shown in Fig. S5. No major changes to 3 %Ni-BiOBr performance after five cycles, which means 3 %Ni-BiOBr has good stability. Fig. S6a and Fig. S6b show the XRD patterns and XPS full spectra of 3 % Ni-BiOBr after five cycles, which show that there is no significant change before and after the reaction. The above results indicate that 3 % Ni-BiOBr has good stability.

Furthermore, in situ FT-IR was applied to probe the intermediate process of CO_2 reduction of 3 % Ni-BiOB. As shown in Fig. 8, there is a distinct peak pack at 1643 cm^{-1} which was attributed to the variable angle vibration of the H_2O [43]. After illumination with a xenon lamp, several bands appeared in the range of 1200–1800 cm^{-1}. The peaks can be specifically attributed to the monodentate carbonate m-CO_3^{2-} (1489 cm^{-1}), the bidentate carbonate b-CO_3^{2-} (1385 cm^{-1}) [44], formate (1748 cm^{-1}), and CO_2 groups (1608 cm^{-1} and 1673 cm^{-1}) [45]. The intensity of m-CO_3^{2-} and b-CO_3^{2-} increases significantly with increasing irradiation time, indicating that CO_2 molecules can adsorb on the surface of the photocatalyst and react with the photogenerated carriers.

CO_2^- can then react with H^+ to form COOH*, which is often considered to be the key intermediate in the reduction of CO_2 to CO [46]. As the reaction time increases, the asymmetric stretching peak of carbon dioxide diminishes, indicating that the carbon dioxide adsorbed on the catalyst surface is gradually reduced to CO.

Based on the above results, the mechanism of photoreduction CO_2 under Ni doping in unit cell of BiOBr to enhance IEF is proposed, as shown in Fig. 9. Under light irradiation, electrons in the valence band (VB) are excited to form hole pairs (e^--h^+). Because of the Ni doping in unit cell of BiOBr enhances the IEF, the photogenerated electrons are pushed to the CB under the strong IEF force. The above process can significantly promote the carrier separation and thus improve the photocatalytic performance. At the same time, $Ru(bpy)_3^{2+}$ is activated to $Ru(byp)_3^{2+*}$ in the presence of light. It is then reduced to $Ru(bpy)_3^{3+}$ by TEOA, which is oxidized to $TEOA^+$ [47]. Next, the electrons of $Ru(bpy)_3^{3+}$ were transferred to 3 %Ni-BiOBr and $Ru(bpy)_3^{3+}$ returned to the initial $Ru(bpy)_3^{2+}$. In addition, carbon dioxide adsorbs on 3 %Ni-BiOBr and accepts CB electrons to form CO, while some H^+ in the system also accepts electrons to form H_2.

4. Conclusion

In summary, we find that Ni doping in unit cell of BiOBr increases the dipole moments of 3 %Ni-BiOBr unit cell along the x, z directions from 0 to 0.04768 and 0.11293 eÅ, respectively. Enhancement of the unit cell dipole moment induces spin polarization to enhance the IEF. Under the powerful driving force of IEF, more photogenerated electrons are pushed to the CB, resulting in a significant increase in photocatalytic performance. Therefore, the CO yield of 3 %Ni-BiOBr reached 378.7 $\mu molg^{-1}h^{-1}$, which is 4.3 times higher than pure BiOBr. This work reveals how to increase the built-in electric field and improve photocatalytic performance by increasing the unit cell dipole moment and inducing spin polarization.

CRediT authorship contribution statement

Yiqiao Wang: Conceptualization, Methodology, Software, Investigation, Writing-Review & Editing, Writing – Original Draft, **Yu Xie:** Supervision, Project administration, Funding acquisition, **Shuohan Yu:** Data curation, **Kai Yang:** Investigation, **Yi Shao:** Investigation, **Laixi Zou:** Data Curation, **Boxiao Zhao:** Investigation, **Zilin Wang:** Investigation, **Yun Ling:** Investigation, **Yong Chen:** Investigation.

Declaration of Competing Interest

The authors declare that they have no known competing financial interests or personal relationships that could have appeared to influence
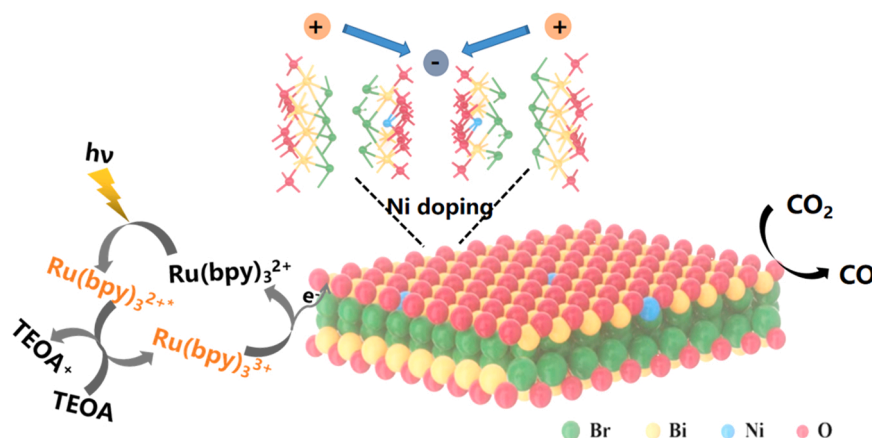

Fig. 9. The schematic CO_2 photoreduction mechanism of 3 %Ni-BiOBr with enhanced electric field.

the work reported in this paper.

Data Availability

The authors do not have permission to share data.

Appendix A. Supporting information

Supplementary data associated with this article can be found in the online version at doi:10.1016/j.apcatb.2023.122420.

References

[1] Y. Chen, D.K. Wang, X.Y. Deng, Z.H. Li, Metal-Organic Frameworks (MOFs) for photocatalytic CO2 reduction, Catal. Sci. Technol. 7 (2017) 4893–4904, https://doi.org/10.1039/c7cy01653k.

[2] J.M. Fu, K.X. Jiang, X.Q. Qiu, J.G. Yu, M. Liu, Product selectivity of photocatalytic CO2 reduction reactions, Mater. Today 32 (2020) 222–243, https://doi.org/10.1016/j.mattod.2019.06.009.

[3] H.W. Lv, P.Y. Li, X.J. Li, A. Chen, R. Sa, H. Zhu, R.H. Wang, Boosting photocatalytic reduction of the diluted CO2 over covalent organic framework, Chem. Eng. J. 451 (2023), 148745, https://doi.org/10.1016/j.cej.2022.148745.

[4] H.Y. Yang, Y.R. Dang, X. Cai, X.N. Bu, J. Li, S.G. Li, Y.H. Sun, P. Gao, Selective synthesis of olefins via CO2 hydrogenation over transition-metal-doped iron-based catalysts, Appl. Catal. B Environ. 321 (2023) 122050, https://doi.org/10.1016/j.apcatb.2022.12205.

[5] R.G. Yang, Y.M. Fu, H.N. Wang, D.P. Zhang, Z. Zhou, Y.Z. Cheng, X. Meng, Y.O. He, Z.M. Su, ZIF-8/covalent organic framework for enhanced CO2 photocatalytic reduction in gas-solid system, Chem. Eng. J. 450 (2022), 138040, https://doi.org/10.1016/j.cej.2022.138040.

[6] J.F. Tian, X. Zhong, X.W. Zhu, X. Yang, J.M. Yang, Z. Mo, J.Y. Liu, J.C. Dai, Y.B. She, Y.H. Song, H.M. Li, H. Xu, Highly exposed active sites of Au nanoclusters for photocatalytic CO2 reduction, Chem. Eng. J. 451 (2023), 138392, https://doi.org/10.1016/j.cej.2022.138392.

[7] H.Z. Wu, Z.Z. Hu, R.H. Liang, O.V. Nkwachukwu, O.A. Arotiba, M.H. Zhou, Novel Bi2Sn2O7 quantum dots/TiO2 nanotube arrays S-scheme heterojunction for enhanced photoelectrocatalytic degradation of sulfamethazine, in: Appl. Catal. B Environ, 321, 2022, p. 122053, https://doi.org/10.1016/j.apcatb.2022.122053.

[8] J.X. Ji, R.R. Li, H. Zhang, Y.N. Duan, Q. Liu, H.Z. Wang, Z.R. Shen, Highly selective photocatalytic reduction of CO2 to ethane over Au-O-Ce sites at micro-interface, Appl. Catal. B Environ. 321 (2022), 122020, https://doi.org/10.1016/j.apcatb.2022.122020.

[9] X.M. Guo, K.L. Gao, W. Zhu, C.H. Liang, Q. Li, F. Fu, Y.F. Zhu, Accurate guided alternating atomic layer enhance internal electric field to steering photogenerated charge separation for enhance photocatalytic activity, Appl. Catal. B Environ. 298 (2021), 120536, https://doi.org/10.1016/j.apcatb.2021.120536.

[10] S.T. Guo, Z.Y. Tang, Y.W. Du, T. Liu, T. Ouyang, Z.Q. Liu, Chlorine anion stabilized Cu2O/ZnO photocathode for selective CO2 reduction to CH4, Appl. Catal. B Environ. 321 (2023), 122035, https://doi.org/10.1016/j.apcatb.2022.122035.

[11] D.J. Mao, S.X. Yang, Y. Hu, H. He, S.G. Yang, S.R. Zheng, C. Sun, Z.F. Jiang, X. L. Qu, P.K. Wong, Efficient CO2 photoreduction triggered by oxygen vacancies in ultrafine Bi5O7 Br nanowires, Appl. Catal. B Environ. 321 (2023) 122201–122031, https://doi.org/10.1016/j.apcatb.2022.

[12] H.X. Zhang, Q.L. Hong, J. Li, F. Wang, X.S. Huang, S.M. Chen, W.G. Tu, D.S. Yu, R. Xu, T.H. Zhou, J. Zhang, Isolated square-planar copper center in boron imidazolate nanocages for photocatalytic reduction of CO2 to CO, Angew. Chem. Int. Ed. 58 (2019) 11752–11756, https://doi.org/10.1002/anie.201905869.

[13] X.W. Xu, T. Tanake, K. Teramura, High selectivity toward CO evolution for the photocatalytic conversion of CO2 by H2O as an electron donor over Ag-loaded β-Ga2O3, Appl. Catal. B Environ. 321 (2022), 122027, https://doi.org/10.1016/j.apcatb.122027.

[14] J.M. Yang, L.Q. Jing, X.W. Zhu, W. Zhang, J.J. Deng, Y.B. She, K.Q. Nie, Y.C. Wei, H.M. Li, H. Xu, Modulating electronic structure of lattice O-modified orange polymeric carbon nitrogen to promote photocatalytic CO2 conversion, Appl. Catal. B Environ. 320 (2023), 122005, https://doi.org/10.1016/j.apcatb.2022.122005.

[15] L. Jin, E. Shaaban, S. Bamonte, D. Cintron, S. Shuster, L. Zhang, G.H. Li, J. He, Surface basicity of Metal@TiO2 to enhance photocatalytic efficiency for CO2 reduction, ACS Appl. Mater. Interfaces 13 (2021) 38595–38603, https://doi.org/10.1021/acsami.1c09119.

[16] X. Chen, Y.J. Chen, X. Liu, Q. Wang, L.G. Li, L.Z. Du, G.H. Tian, Boosted charge transfer and photocatalytic CO2 reduction over sulfur-doped C3N4 porous nanosheets with embedded SnS2-SnO2 nanojunctions, Sci. China Mater. 65 (2022) 400–412, https://doi.org/10.1007/s40843-021-1744-5.

[17] Y. Liu, L. Deng, J.P. Sheng, F.Y. Tang, K. Zeng, L.Q. Wang, K.X. Liang, H. Hu, Y. N. Liu, Photostable core-shell CdS/ZIF-8 composite for enhanced photocatalytic reduction of CO2, Appl. Surf. Sci. 498 (2019), 143899, https://doi.org/10.1016/j.apsusc.2019.143899.

[18] L. Xia, W.X. Zhou, Y.F. Xu, Z.Q. Xia, X.Z. Wang, Q. Yang, G. Xia, S.P. Chen, S. L. Gao, Ferrocene-boosting Zr-MOFs for efficient photocatalytic CO2 reduction: a trade-off between enhancing LMCT and frustrating Lewis acid, Chem. Eng. J. 451 (2023), 138747, https://doi.org/10.1016/j.cej.2022.138747.

[19] Z.L. Wang, B. Cheng, L.Y. Zhang, J.G. Yu, H.Y. Tian, BiOBr/NiO S-scheme heterojunction photocatalyst for CO2 photoreduction, Sol. RRL 6 (2022), 2100587, https://doi.org/10.1002/solr.202100587.

[20] L. Wang, G.P. Liu, B. Wang, X. Chen, C.T. Wang, Z.X. Lin, J.X. Xia, H.M. Li, Oxygen vacancies engineering–mediated BiOBr atomic layers for boosting visible light-driven photocatalytic CO2 reduction, Sol. RRL 5 (2021), 2000480, https://doi.org/10.1002/solr.202000480.

[21] J.N. Qu, Y. Du, P.H. Ji, P.H. Ji, Z.F. Li, N. Jiang, X.Y. Sun, L. Xue, H.Y. Li, G.L. Sun, Cu co-doped BiOBr with improved photocatalytic ability of pollutants degradation, J. Alloy. Compd. 881 (2021), 160391, https://doi.org/10.1016/j.jallcom.2021.160391.

[22] S. Vinoth, A. Pandikumar, Ni integrated S-gC3N4/BiOBr based Type-II heterojunction as a durable catalyst for photoelectrochemical water splitting, Renew. Energ 173 (2021) 507–519, https://doi.org/10.1016/j.renene.2021.03.121.

[23] X. Jin, L. Ye, H. Xie, G. Chen, Bismuth-rich bismuth oxyhalides for environmental and energy photocatalysis, Coord. Chem. Rev. 349 (2017) 84–101, https://doi.org/10.1016/j.ccr.2017.08.010.

[24] D. Kato, K. Hongo, R. Maezono, M. Higashi, H. Kunioku, M. Yabuuchi, H. Suzuki, H. Okajima, C. Zhong, K. Nakano, R. Abe, H. Kageyama, Valence band engineering of layered bismuth oxyhalides toward stable visible-light water splitting: madelung site potential analysis, J. Am. Chem. Soc. 139 (2017) 18725–18731, https://doi.org/10.1021/jacs.7b11497.

[25] X. Chen, X. Zhang, Y.H. Li, M.Y. Qi, J.Y. Li, Z.R. Tang, Z. Zhou, Y.J. Xu, Transition metal doping BiOBr nanosheets with oxygen vacancy and exposed {102} facets for visible light nitrogen fixation, Appl. Catal. B Environ. 281 (2021), 119516, https://doi.org/10.1016/j.apcatb.2020.119516.

[26] M.H. Guan, G.M. Ren, X.C. Zhang, Q.R. Zhang, C.M. Zhang, R. Li, G.M. Fan, Regulating electronic properties of BiOBr to enhance visible light response via 3d transition metals doping: DFT + U calculations, Inter. J. Quantum Chem. 121 (2021), e26568, https://doi.org/10.1002/qua.26568.

[27] Y. Liu, Z.F. Hu, J.C. Yu, Photocatalytic degradation of ibuprofen on S-doped BiOBr, Chemosphere 278 (2021), 130376, https://doi.org/10.1016/j.chemosphere.2021.130376.

[28] J.D. Pack, H.J. Monkhorst, D.L. Freeman, Lithium crystal properties from high-quality Hartree-Fock wave functions, Solid State Commun. 29 (1979) 723–725, https://doi.org/10.1016/0038-1098(79)91014-7.

[29] R.H. Hertwig, W. Koch, On the parameterization of the local correlation functional. What is Becke-3-LYP, Chem. Phys. Lett. 268 (1997) 345–351, https://doi.org/10.1016/s0009-2614(97)00207-8.

[30] B. Delley, From molecules to solids with the DMol3 approach, J. Chem. Phys. 113 (2000) 7756–7764, https://doi.org/10.1063/1.1316015.

[31] J.L. Zhao, Z.R. Miao, Y.F. Zhang, G.G. Wen, L.H. Liu, X.X. Wang, X.Z. Cao, B. Y. Wang, Oxygen vacancy-rich hierarchical BiOBr hollow microspheres with dramatic CO2 photoreduction activity, J. Colloid Interface Sci. 593 (2021) 231–243, https://doi.org/10.1016/j.jcis.2021.02.117.

[32] W. Li, Y. Zou, X. Geng, F. Xiao, G. An, D. Wang, Constructing highly catalytic oxidation over biobr-based hierarchical microspheres: importance of redox potential of doped cations, Mol. Catal. 438 (2017) 19–29, https://doi.org/10.1016/j.mcat.2017.05.017.

[33] Z. Yang, J. Li, F. Cheng, Z. Chen, X. Dong, BiOBr/protonated graphitic C3N4 heterojunctions: intimate interfaces by electrostatic interaction and enhanced photocatalytic activity, J. Alloy. Compd. 634 (2015) 215–222, https://doi.org/10.1016/j.jallcom.2015.02.103.

[34] Y.Y. Wu, H.D. Ji, Q.M. Liu, Z.Y. Sun, P.S. Li, P.R. Ding, M. Guo, X.H. Yi, W.L. Xu, C. C. Wang, S. Gao, Q. Wang, W. Liu, S.W. Chen, Visible light photocatalytic degradation of sulfanilamide enhanced by Mo doping of BiOBr nanoflowers, J. Hazard. Mater. 424 (2022), 127563, https://doi.org/10.1016/j.jhazmat.2021.127563.

[35] X. Zhang, Y. Zhang, Z.Y. Feng, J.M. Zhao, Z.M. Yang, X. Wang, W.S. Wang, Self-accelerating photocharge separation in BiOBr ultrathin nanosheets for boosting photoreversible color switching, Chem. Eng. J. 428 (2022), 131235, https://doi.org/10.1016/j.cej.2021.131235.

[36] X.J. Wang, Y. Zhao, F.T. Li, L.J. Dou, Y.P. Li, J. Zhao, Y.J. Hao, A chelation strategy for in-situ constructing surface oxygen vacancy on {001} facets exposed BiOBr nanosheets, Sci. Rep. 6 (2016) 24918, https://doi.org/10.1038/srep24918.

[37] W.J. Xu, F.L. Lyu, Y.C. Bai, A.Q. Gao, J. Feng, Z.X. Cai, Y.D. Yin, Porous cobalt oxide nanoplates enriched with oxygen vacancies for oxygen evolution reaction, Nano Energy 43 (2018) 110–116, https://doi.org/10.1016/j.nanoen.2017.11.022.

[38] C.Y. Wang, X. Zhang, H.B. Qiu, G.X. Huang, H.Q. Yu, Bi24O31Br10 nanosheets with controllable thickness for visible–light–driven catalytic degradation of tetracycline

hydrochloride, Appl. Catal. B Environ. 205 (2017) 615–623, https://doi.org/10.1016/j.apcatb.2017.01.015.

[39] W.F. Wei, W.X. Chen, D. Lvey, Rock Salt−Spinel structural transformation in anodically electrodeposited Mn−Co−O nanocrystals, Chem. Mater. 20 (2008) 1941–1947, https://doi.org/10.1021/cm703464p.

[40] S. Ahmed, X. Ding, P.P. Murmu, N.N. Bao, R. Liu, J. Kennedy, L. Wang, J. Ding, T. Wu, A. Vinu, J.B. Yi, High coercivity and magnetization in WSe$_2$ by codoping Co and Nb, Small 16 (2020), 1903173, https://doi.org/10.1002/smll.201903173.

[41] N.T. Taylor, F.H. Davies, S.G. Davies, C.J. Price, S.P. Hepplestone, The fundamental mechanism behind colossal permittivity in oxides, Adv. Mater. 31 (2019), 1904746, https://doi.org/10.1002/adma.201904746.

[42] B.F. Li, F. Wei, B. Su, Z. Guo, Z.X. Ding, M.Q. Yang, S.B. Wang, Mesoporous cobalt tungstate nanoparticles for efficient and stable visible-light-driven photocatalytic CO$_2$ reduction, Mater. Today. Energy 24 (2022), 100943, https://doi.org/10.1016/j.mtener.2022.100943.

[43] X. Li, H.P. Jiang, C.C. Ma, Z. Zhu, X.H. Song, X.Y. Li, H.Q. Wang, P.W. Huo, X. B. Chen, Construction of a multi-interfacial-electron transfer scheme for efficient CO$_2$ photoreduction: a case study using CdIn$_2$S$_4$ micro-flower spheres modified with Au nanoparticles and reduced graphene oxide, J. Mater. Chem. A 8 (2020) 18707–18714, https://doi.org/10.1039/d0ta06602h.

[44] L. Yang, X. Bai, J. Shi, X.Y. Du, L. Xu, P.K. Jin, Quasi-full-visible-light absorption by D35-TiO$_2$/g-C$_3$N$_4$ for synergistic persulfate activation towards efficient photodegradation of micropollutants, Appl. Catal. B Environ. 256 (2019), 117759, https://doi.org/10.1016/j.apcatb.2019.117759.

[45] F.L. Wang, T.T. Hou, X. Zhao, W. Yao, R.Q. Fang, K. Shen, Y.W. Li, Ordered macroporous carbonous frameworks implanted with CdS quantum dots for efficient photocatalytic CO$_2$ reduction, Adv. Mater. 33 (2021), 2102690, https://doi.org/10.1002/adma.202102690.

[46] J. Di, C. Chen, C. Zhu, P. SOng, J. Xiong, M.X. Ji, J.D. Zhou, Q.D. Fu, M.Z. Xu, W. Hao, J.X. Xia, S.Z. Li, H.M. Li, Z. Liu, Bismuth vacancy-tuned bismuth oxybromide ultrathin nanosheets toward photocatalytic CO$_2$ reduction, ACS Appl. Mate. Interfaces 11 (2019) 30786–30792, https://doi.org/10.1021/acsami.9b08109.

[47] Z.Z. Yu, K. Yang, C.L. Yu, K.Q. Lu, W.Y. Huang, L. Xu, L.X. Zou, S.B. Wang, Z. Chen, J. Hu, Y. Hou, Y.F. Zhu, Steering unit cell dipole and internal electric field by highly dispersed Er atoms embedded into NiO for efficient CO$_2$ photoreduction, Adv. Funct. Mater. 32 (2022), 2111999, https://doi.org/10.1002/adfm.202111999.